Extraction of mantle discontinuities from teleseismic ambient noise

S. Kato[1], K. Nishida[1]

[1] Earthquake Research Institute, the University of Tokyo

Corresponding author: Shota Kato (skato@eri.u-tokyo.ac.jp)

Key Points:

- The P-S waves at mantle discontinuities were extracted from the ambient noise excited by the ocean swells.
- We developed the source deconvolution method to generalize a receiver function method to P-wave microseisms.
- The migration result of P-S waves was consistent with previous studies, showing the potential of P-wave microseisms to seismic structures.

Orcid id Shota Kato: https://orcid.org/0000-0003-4270-8261

Orcid id Kiwamu Nishida: https://orcid.org/0000-0001-6778-8080

Abstract

Ocean swell activities excite body-wave microseisms that contain information on the Earth's internal structure. Although seismic interferometry is feasible for exploring structures, it faces the problem of spurious phases stemming from an inhomogeneous source distribution. This paper proposes a new method for inferring seismic discontinuity structures beneath receivers using body-wave microseisms. This method considers the excitation sources of body-wave microseisms to be spatially localized and persistent over time. To detect the P-s conversion beneath the receivers, we generalize the receiver function analysis for earthquakes to body-wave microseisms. The resultant receiver functions migrate to the depth section. The detected 410- and 660-km mantle discontinuities are consistent with the results obtained using earthquakes, thereby demonstrating the feasibility of our method for exploring deep-earth interiors. This study is the first step toward body-wave exploration while considering the sources of P-wave microseisms to be isolated events.

Plain Language Summary

The ocean waves excite persistent and random ground motions called microseisms. Since this excitation is independent of seismic activities, this wavefield has information about seismic structures that earthquakes never have. For the deep structure, such as the mantle and core, body-wave microseisms are more suitable than surface-wave microseisms because body-wave microseisms have better sensitivity. Previous studies using body-wave microseisms mainly adopted the cross-correlation analysis known as seismic interferometry. This method assumes that the microseisms are excited everywhere. However, the inhomogeneous source distribution of body-wave microseisms causes artifacts for exploration by seismic interferometry. We developed a new method which circumvents this problem. Assuming that the body-wave microseisms are spatially isolated, this method extracted the P-s converted waves beneath receivers from body-wave microseisms. The 3-Dimensional imaging result of extracted P-s converted waves shows both 410- and 660-km mantle discontinuities, consistent with results using earthquakes. This study shows the potential of body-wave microseisms for exploring the deep earth structure.

1 Introduction

Microseisms are random seismic wavefields with a frequency range of 0.05–0.50 Hz excited by ocean swell activities (e.g., Nishida, 2017) and can be categorized into primary microseisms (PMs; <0.1 Hz) and secondary microseisms (SMs; >0.1 Hz). PMs are excited by topographic coupling between surface ocean gravity waves and seismic waves (Hasselmann, 1963), whereas SMs are excited by the nonlinear effects of surface ocean gravity waves (Longuet-Higgins, 1950). Although Rayleigh and Love waves dominate the SMs, teleseismic P-waves have also been observed (e.g., Gerstoft *et al*., 2008). It has long been understood that these random wavefields represent noise in earthquake seismology.

In the late 2000s, seismic interferometry (SI) turned the noise into a signal elucidating the Earth's internal structures (e.g., Snieder & Larose, 2013). SI is a technique for extracting Green's functions between seismic stations by calculating the cross-correlation of random seismic wavefields of station pairs. SI assumes a homogeneous distribution of noise sources. Because the wavefield is random, only noise sources within the stationary phase regions contribute constructively to the cross-correlation function. Cross-correlation functions converge into Green's functions, representing the wave propagation between station pairs. Because this assumption is more valid for surface waves, surface-wave exploration became widely used in the late 2000s (e.g., Shapiro & Campillo, 2004).

Body-wave exploration using SI has only recently been developed because body-wave extraction is in practice more difficult than surface-wave extraction. One of the reasons for this is the dominance of Rayleigh waves in SMs, owing to excitation at the surface (e.g., Forghani & Snieder, 2010). Moreover, the source localization of P-wave microseisms violates the assumption of a homogeneous source distribution. Source localization causes the emergence of spurious waves in cross-correlation functions, thereby prohibiting the accurate reconstruction of Green's functions (e.g., Pedersen & Colombi, 2018; Li *et al*., 2020). Such studies showed that for estimating seismic structures using P-wave microseisms, considering their source locations is important. Back projection before cross-correlation is one of the possible solutions for improved extraction (e.g., Liu & Shearer, 2022).

This study employs a strategy that is different from SI. Instead of assuming a homogeneous source distribution, P-wave microseisms are assumed to be spatially isolated events (within several hundred kilometers) with persistent excitation (~6 h). We developed a new

method for estimating seismic structures using P waves from the centroid locations of P-wave microseisms, focusing on the P-s conversion beneath the receivers. To detect this conversion, we generalized a receiver function method for earthquake data (e.g., Langston, 1979) to P-wave microseisms. Receiver function analysis using earthquakes sometimes involves narrow azimuthal coverage from inhomogeneous hypocenters. Utilizing P-wave microseisms in the generalized receiver function (gRF) analysis can improve the azimuthal coverage and broaden the illuminated area.

2 Method and analysis

2.1 Data

We used seismograms from 690 seismic stations (Figure 1b) of the high-sensitivity seismograph network (Hi-net: https://doi.org/10.17598/NIED.0003; Okada *et al*., 2014) deployed by the National Research Institute for Earth Science and Disaster Resilience (NIED). The vertical and horizontal components of the velocity meters with a natural frequency of 1 Hz were deployed at the bottom of the boreholes of the stations. We analyzed the data after eliminating the coherent periodic noise originating from the logger (Takagi *et al*., 2015) and correcting for the instrumental response in the time domain (Maeda *et al*., 2011).

To detect the P-s conversion, we analyzed teleseismic P-wave microseisms from 0.10 to 0.25 Hz. Assuming that the excitation sources were persistent in time but localized in space, they were approximated using a persistent vertical single force at the centroid location. Nishida & Takagi (2022) constructed a centroid single-force catalog of P-wave microseisms from 2004 to 2020 using Hi-net data. To construct the catalog, they developed an autofocusing method that utilizes information on both the slowness and wavefront curvature. Although the catalog also includes PP and PKIKP events, the number of events with high signal-to-noise ratios is smaller than that of P events. Accordingly, we mainly focused on P events. Each event in the catalog includes the event date, centroid location, centroid single force, P-wave beam power, and median absolute deviation of the beamforming result. We chose 5,780 P events with high signal-to-noise ratios. The signal-to-noise ratio was defined as the ratio of the P-wave beam power to the median absolute deviation of the beamforming result. The centroid locations of the P-wave microseisms were classified as the Northern Atlantic Ocean, Northern Pacific Ocean, and Southern Pacific

Ocean (Figure. 1). The histogram of epicentral distances revealed peaks at 30–40° and 90–100° (Figure. S1a).

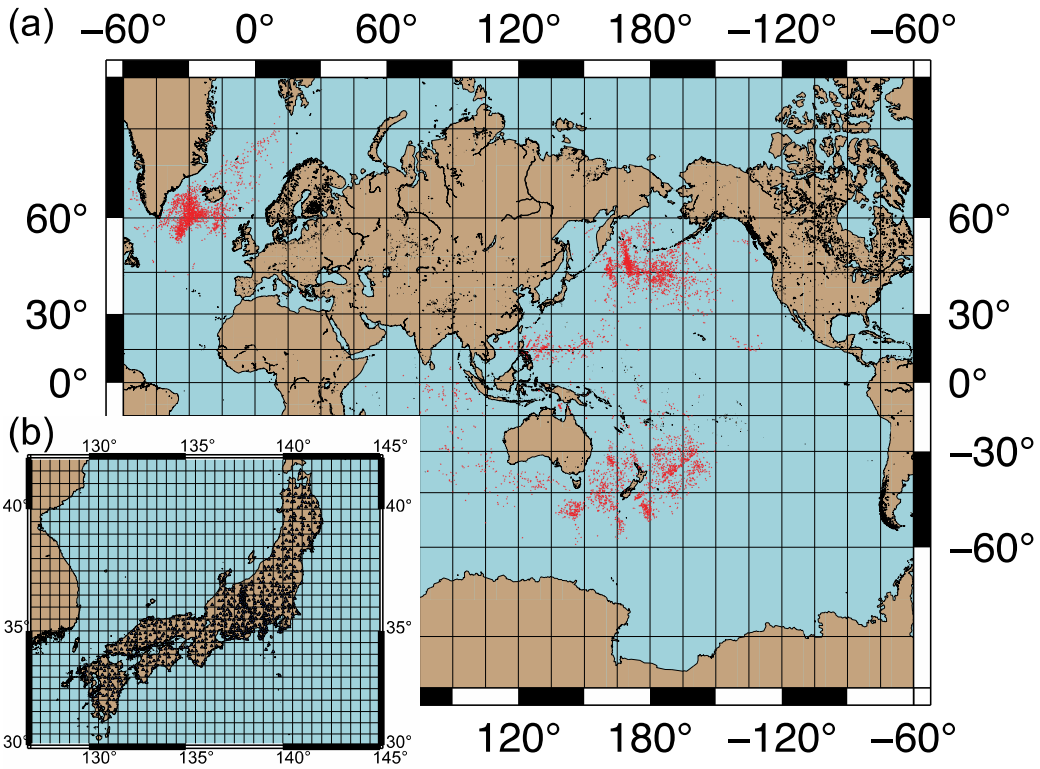

Figure 1. Centroid distribution of the P-wave microseisms used in this study. (**a**) Red dots denote 5,780 P wave source locations (Nishida & Takagi, 2022). (**b**) Blue triangles denote Hi-net stations.

2.2 Calculation of gRFs of P-wave microseisms

The gRF analysis for an earthquake was generalized for persistent P-wave microseisms. The source time function of P-wave microseisms is typically several hours to several days (e.g., Zhang *et al*., 2010), whereas those of most earthquakes are shorter than several minutes. This section describes the procedure for generating gRFs using P-wave microseisms. The centroid location of the P-wave microseisms was fixed at 6 h. Six-hour-long waveforms were split into 1,024-s time windows. We selected time windows with low mean squared amplitudes of 0.05–0.10 Hz (i.e., less than 7.6×10^4 $\mathrm{nm^2/s^2}$) and 0.10–0.20 Hz (i.e., less than 2.5×10^4 $\mathrm{nm^2/s^2}$) to avoid contamination from local earthquakes and suppress local Rayleigh waves. In this frequency range, locally excited Rayleigh waves dominate the records in Japan because

120 teleseismic Rayleigh waves attenuate with propagation owing to scattering and intrinsic
121 attenuation. Indeed, the relative amplitude of P waves to Rayleigh waves is anti-correlated with
122 the mean squared amplitude in the 0.1–0.2 Hz range in Japan (Takagi *et al*., 2018). Although
123 data selection according to the H/V ratio at inland stations is feasible for enhancing teleseismic
124 P-wave microseisms (e.g., Pedersen *et al*., 2023), we chose data with a low mean squared
125 amplitude.

126 For each time step, the Fourier spectrum of the source time function of the incident P
127 wave $P(\omega)$ was estimated by stacking vertical components all over the stations, along with the
128 theoretical P wave travel time. Stacking the vertical components of all stations enhanced the
129 relative amplitude of body waves to Rayleigh waves. The theoretical P wave travel time T_{ip} was
130 calculated using the tauP toolkit (Crotwell *et al*., 1999) for the 1-D velocity model AK135
131 (Kennett *et al*., 1995), with correction for the 3-D velocity model (0–80 km depth) beneath Japan
132 (Nishida *et al*., 2008), assuming a near-vertical incident. The Fourier spectrum of the source time
133 function of the j-th time step is given by

$$P_j(\omega) = \frac{1}{N}\sum_{i=1}^{N} Z_{ij}(\omega)e^{-i\omega T_{ip}},$$

134 where N is the number of seismic stations and Z_{ij} is the vertical component of the j-th time
135 window at the i-th station.

136 The gRF of P-wave microseisms RF_i is calculated by minimizing the squared difference
137 between the radial component of the i-th station and j-th time window R_{ij} and $RF_i \cdot P_j$. Thus, the
138 radial gRF of P-wave microseisms RF_i is calculated as

$$RF_i(\omega) = \frac{\langle R_{ij}{P_j}^* \rangle}{max\left(\langle P_j{P_j}^* \rangle, w \cdot max\langle P_j{P_j}^* \rangle\right)},$$

139 where w is the 5% water level to avoid instability, $max\langle P_j{P_j}^* \rangle$ is the peak value of the power
140 spectrum, and the angle brackets refer to the ensemble average of all the available time windows.
141 The numerator is the power spectrum of the incident P wave, whereas the dominator is the cross-
142 spectrum of the incident P wave P_j and the radial component R_{ij}. In the case of only a one-time

143 window, this equation is equivalent to the typical receiver function including the water level. The
144 vertical component of the gRF is calculated in the same manner.

145 All the radial gRFs for all events were linearly binned-stacked to enhance the signal-to-
146 noise ratio. The width of distance bin was 25 km. All radial gRFs RF_i were normalized by the
147 peak amplitude of the vertical gRFs ZF_i, and aligned at the peak time of ZF_i (e.g., Zhang *et al*.,
148 2010). Quality control of the gRFs was performed before stacking, rejecting those with large
149 amplitudes of 50–500 s before the P peak. The radial gRFs using PP events were calculated in
150 the same manner, while those using PKIKP events were calculated in a slightly different manner
151 (Supporting Information). Because the number of events was less than the number of P events,
152 results are shown in the Supporting Information (Figure S3–S6).

153 **3 Results and Discussion**

154 3.1 Binned stack of gRFs

155 The binned stack of radial gRFs shows the P-s converted waves at the mantle
156 discontinuities with an epicentral distance of 3,000–11,000 km (Figure 2). The relative arrival
157 times of these waves were consistent with the theoretical travel times of AK135.

158 The sidelobe of P waves varies with the epicentral distance because the peak frequency of
159 SMs is affected by the ocean depth in the source area because of the resonance of the water layer
160 (e.g., Gualtieri *et al*., 2014). The amplitude variation of vertical gRFs before the P peaks depends
161 on the stacking number (Figure S2). The binned stack of the vertical gRFs shows no clear PP-
162 and P-reflected waves at the mantle discontinuities (PP410P/PP660P).

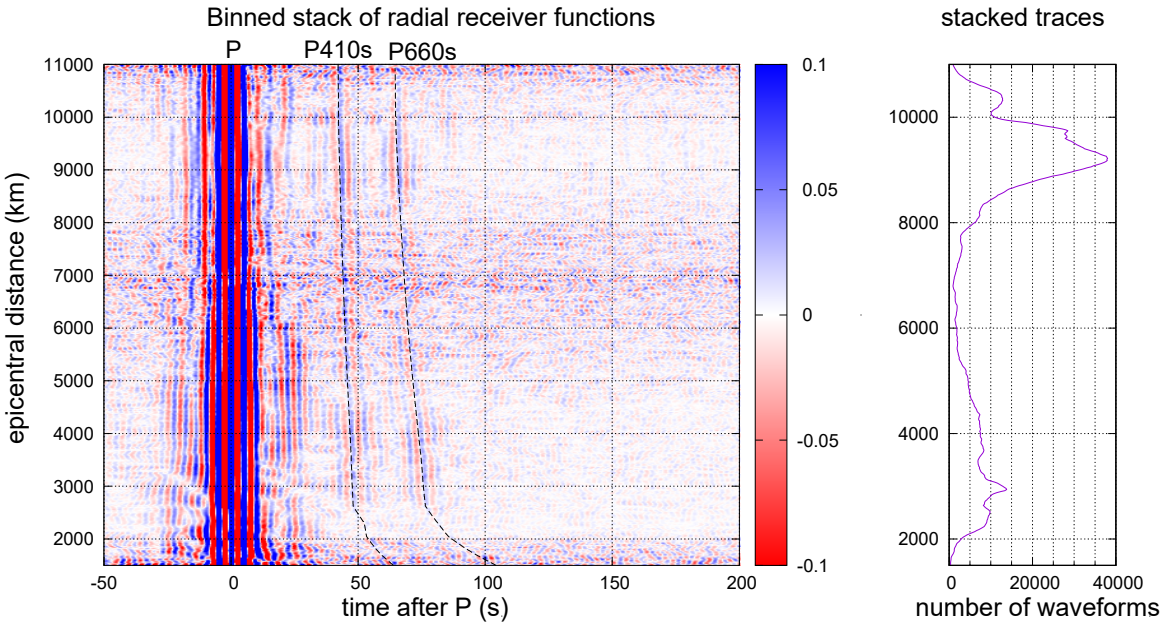

Figure 2. Binned stack of all the radial gRFs of all seismic stations. Each stacked trace is normalized by the maximum value. The peak at the 0 s is the P wave. Two dashed lines show the theoretical travel times of P410s and P660s from AK135. The figure shows these phases along each line. The right panel shows the number of radial gRFs used in the binned stack.

Possible reasons for the emergence of P-s converted phases in the radial components and the lack of these reflection phases in the vertical components are as follows: First, the reflection phases being included in the source time function because of a small difference between the PP410P and PP660P slowness and that of P (~0.0005 s/km with an epicentral distance of 80°); and second, the reverberation at the bounce point causing destructive interference for the reflected phases. However, the P-s converted phases were free of these reasons.

3.2 1-D depth migration

All the radial gRFs were depth-migrated with the 1-D structure of AK135. Assuming that the radial gRFs consist of P-s converted waves, all gRFs with epicentral distances greater than 30° were stacked along the theoretical travel time of the P-s converted waves at depths of 200–1000 km. Travel time was calculated using the tauP toolkit (Crotwell *et al*., 1999). Four groups (all events, Northern Atlantic events, Northern Pacific events, and Southern Pacific events) of gRFs were depth-migrated (Figure 3). At a shallow depth (200 km), results were characterized

by large amplitudes, which can be explained by contamination by the sidelobe of the direct P. All results showed common positive peaks around the depths of 410 and 660 km. The peak depth was somewhat shallow because of the difference in the crustal structure between Japan and AK135.

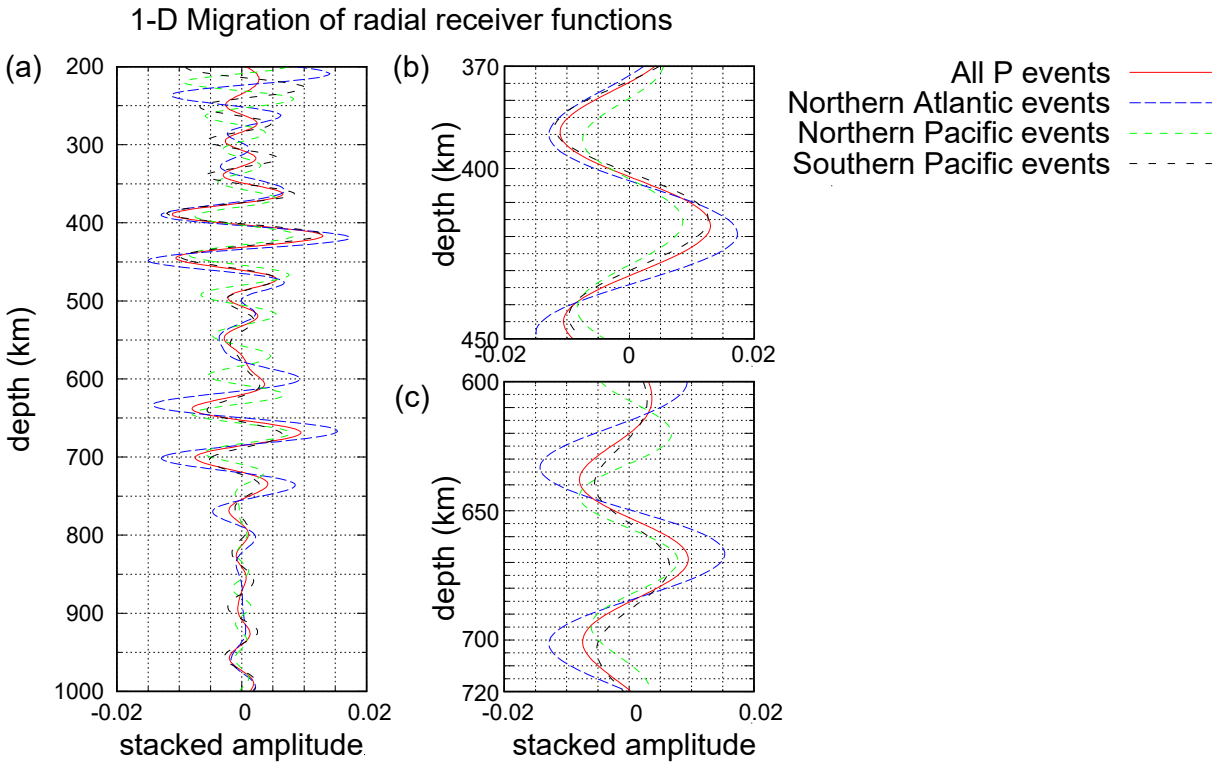

Figure 3. (**a**) Depth migration result of the radial gRFs converted from 200 to 1,000 km depth. Red, blue, green, and black lines indicate the results using all the events, events in the Northern Atlantic, events in the Northern Pacific, and events in the Southern Pacific, respectively. Peaks exist around the depths of 410 and 660 km. (**b**) Enlarged view in the 370–450 km depth range in panel a. (**c**) Enlarged view in the 600–720 km depth range in panel a.

The amplitudes of the P-s waves were compared to previous seismic observations. The P-s transmission coefficients estimated using Japanese broadband stations are 2.7 ± 0.8% and 6.0 ± 0.7% (Kato & Kawakatsu, 2001), while using the PREM parameters (Dziewonski & Anderson, 1981), they are 1.5% and 4.6% (slowness is 0.06 s/km). In this study, we obtained the P-s transmission coefficients of the 410- and 660-km discontinuities as 0.8–1.8% and 0.7–1.5%, respectively. These values are smaller than those reported in previous studies, with the P-s

197 transmission coefficient at 660 km depth being smaller than that at 410 km depth. Waveform
198 distortion due to the high water level during deconvolution may decrease the amplitude of P-s
199 converted waves. However, waveform distortion alone cannot explain the smaller amplitude of
200 P660s compared with that of P410s. A plausible reason is the sharpness of the 410- and 660-km
201 discontinuities, i.e., the frequency dependence of the P-s transmission coefficients because this
202 study used a relatively higher frequency band (0.10–0.25 Hz) than those in previous studies
203 (0.005–0.200 Hz). The widths of the mantle discontinuities may be related to the water content
204 of the transition zone (e.g., Helffrich & Wood, 1996). Our results are consistent with the
205 observed frequency dependence of the P-s conversion at the 660 km discontinuity reported
206 previously (Tonegawa *et al*., 2005). Another possible reason is that the depression of the 660-km
207 discontinuity (a ~40 km depression in southwest Japan; Tono *et al*., 2005; Tonegawa *et al*.,
208 2006) may make P660s incoherent for stacking.

209 3.3 3-D depth migration

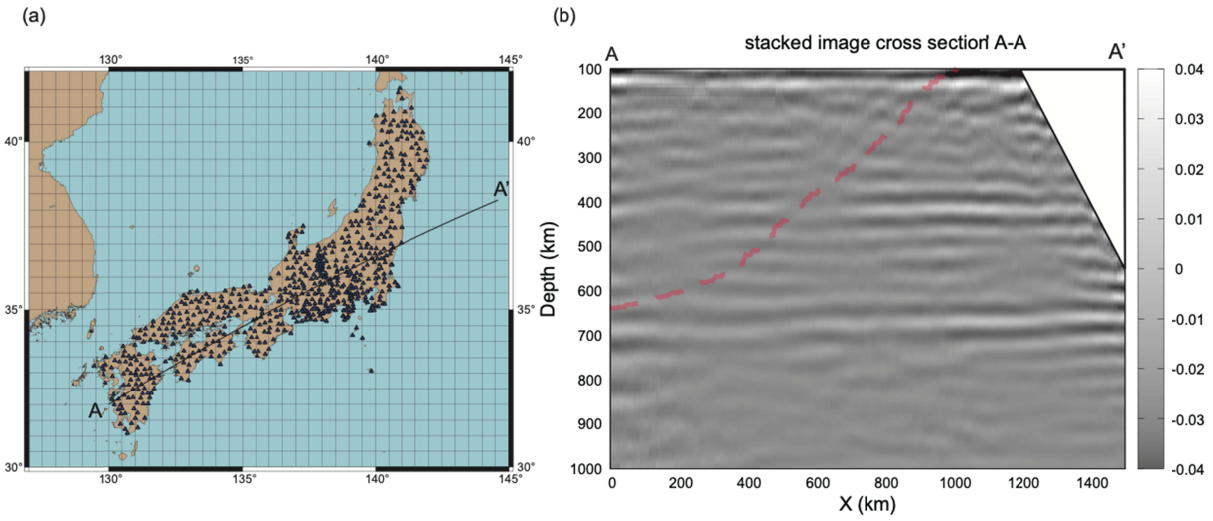

210

211 **Figure 4.** Cross-section (A–A') of the depth-projected radial gRFs. (**a**) Locations of the cross-
212 section and stations (blue triangles) used in this study. (**b**) Stacked image of the A–A' cross-
213 section from 100 to 1,000 km depth. The red line denotes the depth of the top of Pacific slabs
214 (Nakajima & Hasegawa, 2006; Nakajima *et al*., 2009). The shallow part near A' is muted due to
215 the poor ray path coverage.

The migration of all the radial gRFs with the 3-D structure was calculated. Assuming that the radial gRFs consisted of P-s converted waves, all the gRFs with epicentral distances greater than 30° were projected to the 100–1,000 km depth domain. Figure 4 shows a cross-section using these depth-projected gRFs. At each point on the cross-section, the gRFs were stacked with a horizontal distance smaller than 1°. The image of the cross-section shows the horizontally continuous 410- and 660-km discontinuities. The 410-km discontinuity has a gap where the Pacific plate (red line in the figure) crosses the 410-km depth. The 660-km discontinuity is depressed where the Pacific slab stagnates above the 660-km discontinuity. However, the Pacific plate is not evident in the cross-section because the spatial stacking length is too large to image the subducting plate surface (Kawakatsu & Yoshioka, 2011).

The cross-section from the resultant gRFs was compared with the stacked image from conventional receiver functions using an earthquake (Tonegawa *et al*., 2006). Because the locations of both the cross-section and frequency band are similar, the cross-section of Tonegawa *et al.* (2006) is adequate for reference. The signatures of the mantle discontinuities were common in both images, demonstrating the reliability of this method.

3.4 Applicability of this method to other seismic arrays

The relative amplitude of body waves to surface waves of microseisms is one of the factors determining the signal-to-noise ratio in this method. The waveforms of the Hi-net stations are dominated by surface waves excited by the sea around Japan, whereas those of stations in the continental region are less dominated by surface waves owing to scattering decay (e.g., Vinnik, 1973). An inland array is preferable; however, our method still requires more than 500 stations to accurately extract the incident P-wave microseism. It also requires long-term observations, with time periods of over 10 years, and a sufficient number of events. Because dense observations have become popular in the last decade, our method could be feasible for extracting P-s converted waves using seismic networks on the continent.

4 Conclusions

We performed a generalized receiver function analysis of P-wave microseisms. Contrary to the SI assumption, this method assumes that the sources of body-wave microseisms are persistent in time and spatially localized. This strategy constitutes a solution to the spurious phase problem of body-wave extraction using SI. The resultant migration image showed the extraction of the P410s/P660s from the radial gRFs. The stacked image from the extracted P-s converted waves was consistent with the images from the conventional receiver function analysis using earthquakes. The results demonstrate the feasibility of our method using body-wave microseisms for exploring the Earth's deep interior, while this method can also be applied to other modern arrays. This study is the first step toward seismic exploration while considering the sources of P-wave microseisms to be isolated events; it has the potential to extract information not only from the receiver side, but also along the path, including the source side.

Acknowledgments

We are grateful to all the people maintaining the Hi-net stations and making the waveforms readily available. We thank Takashi Tonegawa and Ryota Takagi for their valuable discussions. Data pre-processing was performed using ObsPy (Krischer *et al*., 2015). Figures were generated using Generic Mapping Tools (Wessel *et al*., 2019). K. Nishida was supported by JSPS KAKENHI (Grant No. 21K03715).

Open Research

We used data from Hi-net (https://doi.org/10.17598/nied.0003) managed by the National Research Institute for Earth Science and Disaster Prevention (NIED), Japan.

The CSF catalog in this study is available on the Zenodo web page https://zenodo.org/record/6001637 (Nishida, 2022).

Reference

Crotwell, H. P., Owens, T. J., & Ritsema, J. (1999). The TauP Toolkit: Flexible Seismic Travel-time and Ray-path Utilities. *Seismological Research Letters*, *70*(2), 154–160.

Dziewonski, A. M., & Anderson, D. L. (1981). Preliminary reference Earth model. *Physics of the Earth and Planetary Interiors*, *25*(4), 297–356.

Forghani, F., & Snieder, R. (2010). Underestimation of body waves and feasibility of surface-wave reconstruction by seismic interferometry. *Leading Edge*, *29*(7), 790–794.

Gerstoft, P., Shearer, P. M., Harmon, N., & Zhang, J. (2008). Global P, PP, and PKP wave microseisms observed from distant storms. *Geophysical Research Letters*, *35*(23). https://doi.org/10.1029/2008gl036111

Gualtieri, L., Stutzmann, E., Farra, V., Capdeville, Y., Schimmel, M., Ardhuin, F., & Morelli, A. (2014). Modelling the ocean site effect on seismic noise body waves. *Geophysical Journal International*, *197*(2), 1096–1106.

Hasselmann, K. (1963). A statistical analysis of the generation of microseisms. *Reviews of Geophysics (Washington, D.C.: 1985)*, *1*(2), 177.

Helffrich, G. R., & Wood, B. J. (1996). 410 km discontinuity sharpness and the form of the olivine α-β phase diagram: resolution of apparent seismic contradictions. *Geophysical Journal International*, *126*(2), F7–F12.

Kato, M., & Kawakatsu, H. (2001). Seismological in situ estimation of density jumps across the transition zone discontinuities beneath Japan. *Geophysical Research Letters*, *28*(13), 2541–2544.

Kawakatsu, H., & Yoshioka, S. (2011). Metastable olivine wedge and deep dry cold slab beneath southwest Japan. *Earth and Planetary Science Letters*, *303*(1–2), 1–10.

Kennett, B. L. N., Engdahl, E. R., & Buland, R. (1995). Constraints on seismic velocities in the Earth from traveltimes. *Geophysical Journal International*, *122*(1), 108–124.

Krischer, L., Megies, T., Barsch, R., Beyreuther, M., Lecocq, T., Caudron, C., & Wassermann, J. (2015). ObsPy: a bridge for seismology into the scientific Python ecosystem. *Computational Science & Discovery*, *8*(1), 014003.

Langston, C. A. (1979). Structure under Mount Rainier, Washington, inferred from teleseismic body waves. *Journal of Geophysical Research, [Solid Earth]*, *84*(B9), 4749–4762.

Li, L., Boué, P., & Campillo, M. (2020). Observation and explanation of spurious seismic signals emerging in teleseismic noise correlations. *Solid Earth*, *11*(1), 173–184.

Liu, T., & Shearer, P. M. (2022). Likely P - to - S conversion at the core - mantle boundary extracted from array processing of noise records. *Geophysical Research Letters*, *49*(7). https://doi.org/10.1029/2021gl097034

Longuet-Higgins, M. S. (1950). A theory of the origin of microseisms. *Philosophical Transactions of the Royal Society of London. Series A: Mathematical and Physical Sciences*, *243*(857), 1–35.

Maeda, T., Obara, K., Furumura, T., & Saito, T. (2011). Interference of long-period seismic wavefield observed by the dense Hi-net array in Japan. *Journal of Geophysical Research, [Solid Earth]*, *116*(B10). https://doi.org/10.1029/2011JB008464

Nakajima, J., & Hasegawa, A. (2006). Anomalous low-velocity zone and linear alignment of seismicity along it in the subducted Pacific slab beneath Kanto, Japan: Reactivation of subducted fracture zone? *Geophysical Research Letters*, *33*(16). https://doi.org/10.1029/2006GL026773

Nakajima, J., Hirose, F., & Hasegawa, A. (2009). Seismotectonics beneath the Tokyo metropolitan area, Japan: Effect of slab-slab contact and overlap on seismicity. *Journal of Geophysical Research, [Solid Earth]*, *114*(B8). https://doi.org/10.1029/2008JB006101

Nishida, K., Kawakatsu, H., & Obara, K. (2008). Three-dimensional crustal S wave velocity structure in Japan using microseismic data recorded by Hi-net tiltmeters. *Journal of Geophysical Research, [Solid Earth]*, *113*(B10). https://doi.org/10.1029/2007JB005395

Nishida, K. (2017). Ambient seismic wave field. *Proceedings of the Japan Academy. Series B, Physical and Biological Sciences*, *93*(7), 423–448.

Nishida, K, & Takagi, R. (2022). A Global Centroid Single Force Catalog of P-Wave Microseisms. *Journal of Geophysical Research, [Solid Earth]*, *127*(4), e2021JB023484.

315 Okada, Y., Kasahara, K., Hori, S., Obara, K., Sekiguchi, S., Fujiwara, H., & Yamamoto, A. (2014). Recent progress
316 of seismic observation networks in Japan —Hi-net, F-net, K-NET and KiK-net—. *Earth, Planets and*
317 *Space*, *56*(8), xv–xxviii.
318 Pedersen, H. A., & Colombi, A. (2018). Body waves from a single source area observed in noise correlations at
319 arrival times of reflections from the 410 discontinuity. *Geophysical Journal International*, *214*(2), 1125–
320 1135.
321 Pedersen, H. A., Mattern, F., & Poli, P. (2023). Imaging with seismic noise: improving extraction of body wave
322 phases from the deep Earth through selective stacking based on H/V ratios. *Geophysical Journal*. Retrieved
323 from https://academic.oup.com/gji/article-abstract/232/2/1455/6750232
324 Shapiro, N. M., & Campillo, M. (2004). Emergence of broadband Rayleigh waves from correlations of the ambient
325 seismic noise. *Geophysical Research Letters*, *31*(7). https://doi.org/10.1029/2004GL019491
326 Snieder, R., & Larose, E. (2013). Extracting Earth's Elastic Wave Response from Noise Measurements. *Annual*
327 *Review of Earth and Planetary Sciences*, *41*(1), 183–206.
328 Takagi, R., Nishida, K., Aoki, Y., Maeda, T., Masuda, K., Takeo, M., et al. (2015). A Single Bit Matters: Coherent
329 Noise of Seismic Data Loggers. *Seismological Research Letters*, *86*(3), 901–907.
330 Takagi, R., Nishida, K., Maeda, T., & Obara, K. (2018). Ambient seismic noise wavefield in Japan characterized by
331 polarization analysis of Hi-net records. *Geophysical Journal International*, *215*(3), 1682–1699.
332 Tonegawa, T., Hirahara, K., & Shibutani, T. (2005). Detailed structure of the upper mantle discontinuities around
333 the Japan subduction zone imaged by receiver function analyses. *Earth, Planets, and Space: EPS*, *57*(1), 5–
334 14.
335 Tonegawa, T., Hirahara, K., Shibutani, T., & Shiomi, K. (2006). Upper mantle imaging beneath the Japan Islands by
336 Hi-net tiltmeter recordings. *Earth, Planets and Space*, *58*(8), 1007–1012.
337 Tono, Y., Kunugi, T., Fukao, Y., Tsuboi, S., Kanjo, K., & Kasahara, K. (2005). Mapping of the 410- and 660-km
338 discontinuities beneath the Japanese islands. *Journal of Geophysical Research, [Solid Earth]*, *110*(B3).
339 https://doi.org/10.1029/2004JB003266
340 Vinnik, L. P. (1973). Sources of microseismicP waves. *Pure and Applied Geophysics*, *103*(1), 282–289.
341 Wessel, P., Luis, J. F., Uieda, L., Scharroo, R., Wobbe, F., Smith, W. H. F., & Tian, D. (2019). The generic mapping
342 tools version 6. *Geochemistry, Geophysics, Geosystems*, *20*(11), 5556–5564.

Zhang, J., Gerstoft, P., & Shearer, P. M. (2010). Resolving P-wave travel-time anomalies using seismic array observations of oceanic storms. *Earth and Planetary Science Letters*. Retrieved from https://www.sciencedirect.com/science/article/pii/S0012821X10001160

Reference from the Supporting Information

Takagi, R., Toyokuni, G., & Chikasada, N. (2020). Ambient noise correlation analysis of S-net records: extracting surface wave signals below instrument noise levels. *Geophysical Journal International*, *224*(3), 1640–1657.